Low-Profile Switched-Beam Antenna Backed by an Artificial Magnetic Conductor for Efficient Close-to-Metal Operation

Gregor Lasser, *Member, IEEE*, Lukas W. Mayer, Zoya Popović, *Fellow, IEEE*, and Christoph F. Mecklenbräuker, *Senior Member, IEEE*

***Abstract*—This paper presents a compact switched-beam antenna (SBA) mounted on the bottom of a car. The antenna and associated circuits read RFID data sensed directly from all four tires. The frequencies of interest are the European UHF RFID band (866 MHz) and the 2.45 GHz ISM-band. In both cases, the antenna is electrically close to the conductive floor of the vehicle. In order to improve performance, dual-band periodic printed surfaces are designed and the efficiency, pattern, and loss are characterized for the antenna mounted above the FSS. In the UHF-band, the size of the assembly is $0.87\lambda_0 \times 0.87\lambda_0 \times 0.11\lambda_0$ and its performance is not sensitive to the position of the conductive car bottom surface. The antenna over FSS assembly has a directivity of 5.6 dB and the efficiency is enhanced by a factor of 2.35 (3.7 dB).**

***Index Terms*—Antennas, beam steering, efficiency, frequency selective surfaces, metamaterials, radio-frequency identification.**

I. Introduction

ACTIVE tire pressure monitors in vehicles employ an onboard unit (OU), which communicates with sensor nodes in the wheels. These are usually mounted on the rim and powered by a battery [1] and operate in the UHF range (315 or 433 MHz). In advanced tire monitoring systems, the sensor is in the tire and capable of collecting additional data such as temperature and vibration from which the contact area can be estimated [2]. Such sensors can be implemented using radio-frequency identification (RFID) technology to eliminate the need for batteries. The acquired tire sensor information extends classical active safety systems like electronic stability control (ESC) [3]. However, the rubber and metal in the tires have high attenuation [4], resulting in poor RFID antenna performance. Additionally, the losses and reflections between the metal car and the road make the communication channel between the onboard unit and the RFID-based sensor very poor [5]. The radiation pattern of the tire–antenna assembly is determined by the orientation of the antenna in the tire [6], potentially deteriorating the communication link [7].

Fig. 1 shows a sketch of the desired RFID OU antenna position. A reconfigurable OU antenna which steers the antenna beam toward one wheel at a time is desirable for two reasons. The directive beam improves the communication channel for both forward and reverse (backscattered) links. Furthermore, this minimizes the cross talk between RFID sensors associated with the remaining wheels [8]. This in turn reduces the required power and simplifies sensor tagging. The OU antenna should be placed centrally between the wheels, and for manufacturability and ease of integration with the electronics, we desire a printed antenna which can be placed parallel to the ground and close to the metal vehicle body. Since the vehicle floor pan is usually constructed from steel, such a printed antenna will suffer from a mostly reactive impedance difficult to match, and degraded efficiency and radiation patterns. Therefore, in this paper, a periodic frequency selective surface (FSS) that is placed between the antenna and car floor is presented, with the goal of shielding the antenna from the metal part of the vehicle while maintaining a low overall antenna profile.

Such a FSS needs to have a plane wave reflection phase close to 0° and is referred to as an artificial magnetic conductor (AMC). While the size of a unit cell of many AMCs is in the order of half a free-space wavelength λ_0 [9], [10], the unit cell dimensions presented here are smaller than $\lambda_0/17$ at 868 MHz resulting in a closer approximation to a homogeneous artificial surface impedance.

In the following section, we briefly explain the switched beam antenna (SBA) in its two configurations: 1) for the European UHF RFID band at 866 MHz and 2) for the 2.45-GHz ISM-band. This section is followed by a description of the developed AMC surface suitable for both frequency bands. In Section IV, we will present measurement results of the SBA mounted atop the designed AMC surface, including return loss, radiation pattern, and efficiency.

II. Switched Beam Antenna

The goal is to create a compact antenna which can steer an equal beam in all four azimuth sectors. SBAs are covered in many publications, but most deal with large phased arrays, exceptions being [11]–[14]. The configuration described in [14] is in some aspects similar to the configuration discussed in this

Manuscript received February 24, 2015; revised September 30, 2015; accepted December 02, 2015. Date of publication February 05, 2016; date of current version April 05, 2016. This work was supported by the Christian Doppler Laboratory for Wireless Technologies for Sustainable Mobility.

G. Lasser and Z. Popović are with the Department of Electrical, Computer, and Energy Engineering, University of Colorado Boulder, Boulder, CO 80309 USA (e-mail: gregor.lasser@colorado.edu).

L. W. Mayer and C. F. Mecklenbräuker are with the Christian Doppler Laboratory for Wireless Technologies for Sustainable Mobility, Institute of Telecommunications, Vienna University of Technology, Vienna 1040, Austria.

Color versions of one or more of the figures in this paper are available online at http://ieeexplore.ieee.org.

Digital Object Identifier 10.1109/TAP.2016.2526044

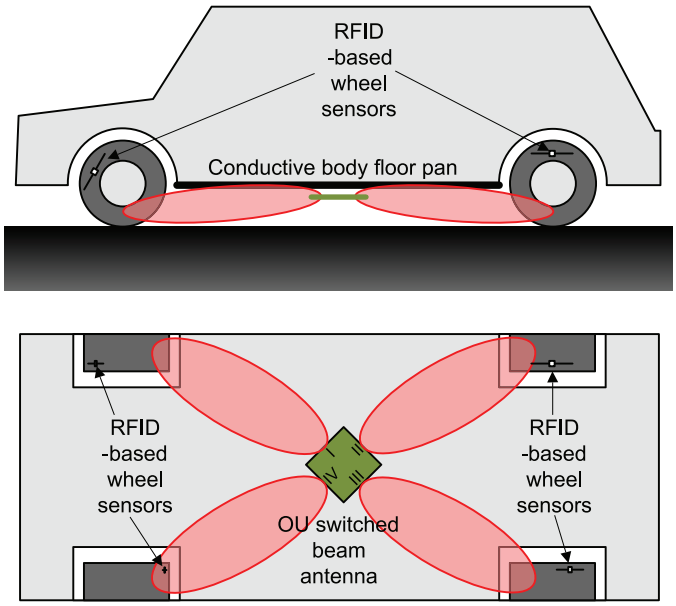

Fig. 1. Sketch of the RFID-based tire pressure monitoring system. The on-board unit (OU) contains the RFID reader, which has an SBA that points in the direction of one wheel at a time in order to reduce the channel loss and the interference from other sensor nodes.

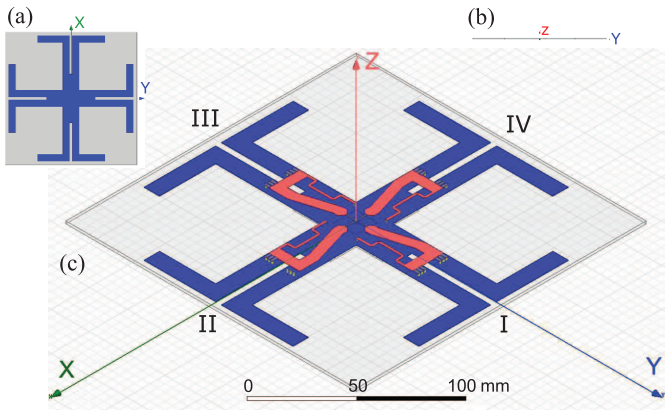

Fig. 2. Antenna geometry of the UHF-SBA for simulation showing feeding side in red (bright) and dipole side in blue (dark). (a) Bottom view, (b) side view, and (c) perspective view showing beam numbers in roman numerals.

contribution. The antenna itself has similar dimensions with respect to the wavelength and it is operated close to a FSS. However, our antenna uses a single feeding point and is operational in free space, while the design in [14] relies on a modified Sievenpiper structure. Furthermore, these patch elements have an edge length in the order of half a wavelength prohibiting the homogeneous surface assumption of the FSS. Section III describes techniques to reduce the size of a unit cell to 0.058 λ_0 at 868 MHz and 0.163 λ_0 at 2.45 GHz. Furthermore, our unit cells are identical, whereas [14] uses vias only at the outer cells of the FSS aimed at reducing surface waves.

Both versions of our SBA are fabricated on a printed circuit board (PCB) that contains four dipoles with balanced centrally shorted lines on the one side, and the feeding network on the other side, as can be seen in Fig. 2. For normal operation, only one dipole is fed, whereas the three other dipoles are deactivated by shorting their feed lines. The directivity of the antenna

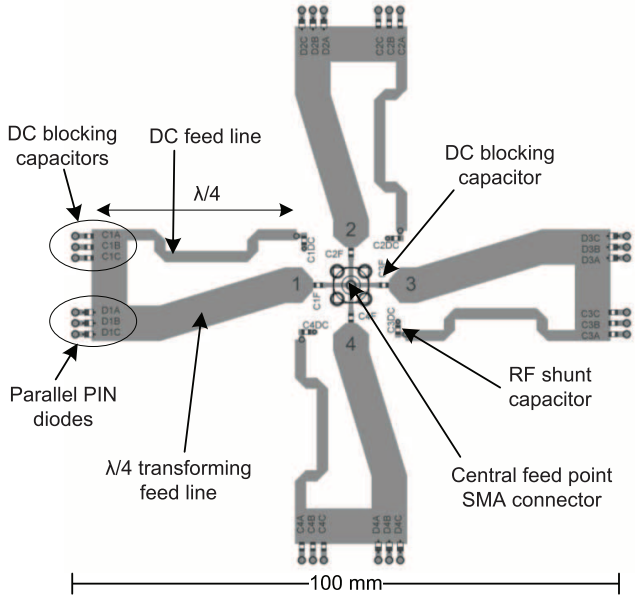

Fig. 3. Feeding network of the UHF-SBA including discrete components.

is based on the fact that the balanced lines connecting the neighboring deactivated dipoles act as a reflector for the driven element.

A. UHF-Band Antenna

The UHF version of this antenna was initially published in [8]. It is constructed on a PCB of FR-4 material with dimensions 190 × 190 mm or $0.55\,\lambda_0 \times 0.55\,\lambda_0$ and a thickness of 1.5 mm. The feeding network is shown in Fig. 3. From the central feed point short thin transmission lines connect to DC blocking capacitors which lead to low-impedance microstrip lines departing toward the PIN diodes. The overall electrical length from the feed point to the PIN diodes corresponds to a quarter of a guided wavelength $\lambda/4$. The low-impedance lines transform the 50-Ω impedance of the coaxial cable to the lower impedance required at the symmetric feed point of a single dipole element. Additionally, this line acts as a balun to convert the asymmetric microstrip line to the balanced dipole feed. At the end of the $\lambda/4$ feedline, three PIN diodes are connected in parallel to create an appropriate low inductance short, which deactivates the corresponding dipole. For the same reason, to reduce inductance, the balanced dipole feed is connected to the feedline with three vias and three DC blocking capacitors in parallel. The biasing circuit for the PIN diodes is a high-impedance quarter wavelength transmission line with an RF short capacitor. The DC signal is applied at this point through a via that is routed to an additional small biasing control PCB at the center of the antenna. Since this PCB is only covering parts of the antenna which are also covered by the central ground plane of the dipole layer, it does not influence the antenna properties.

The measured gain pattern corresponding to E_φ of this antenna is plotted in Fig. 4, with the coordinate system as shown in Fig. 2. When the beam is pointed in y direction, a peak at $\varphi = 90°$ is created. Switching to different beams will

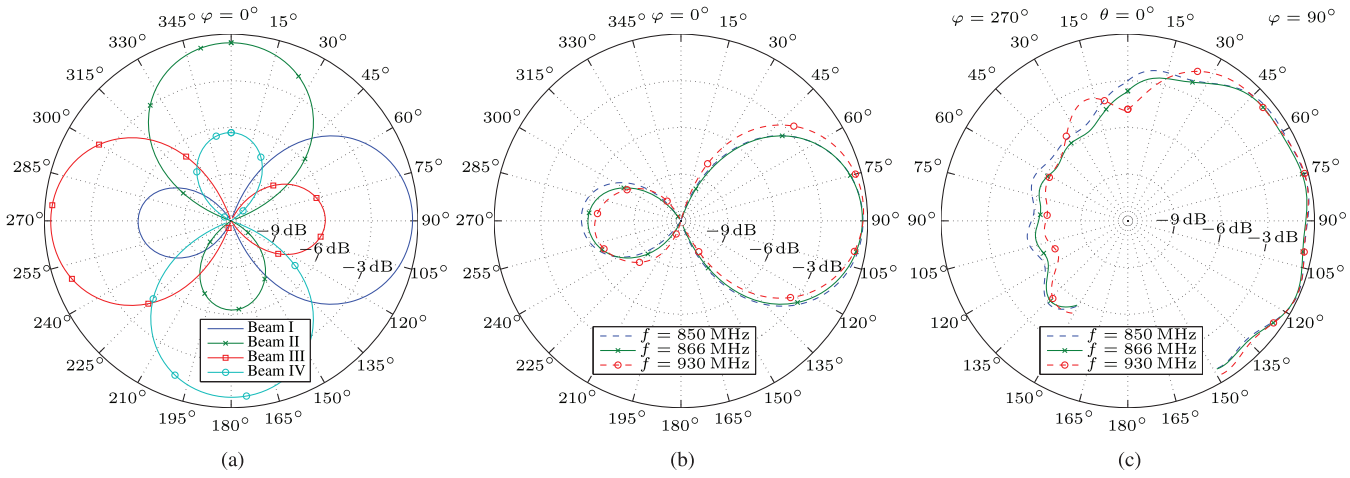

Fig. 4. Normalized gain patterns corresponding to E_φ for the UHF-SBA in free space. (a) Azimuth beam comparison. (b) Azimuth cut for three frequencies and beam I at $\theta = 90°$. Polar cut for three frequencies and beam I. For beam orientation, see Fig. 2.

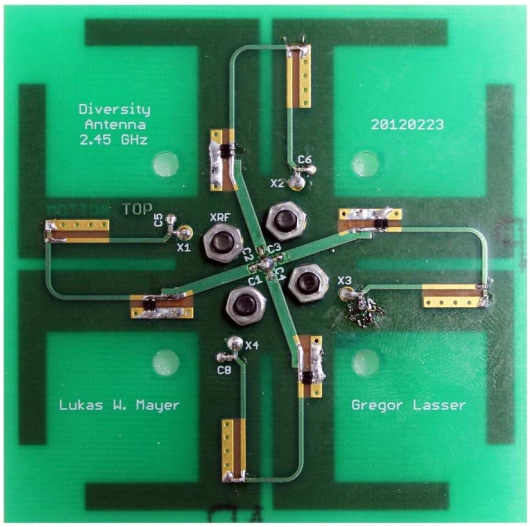

Fig. 5. Photograph of the manufactured ISM-SBA feed side printed to scale (1:1). The dipole side can be seen through the semitransparent FR-4 printed surface board material. The four screws attach a standard SMA flange from the opposite side to the antenna PCB.

produce peaks at $\varphi = 0°, 90°, 180°,$ and $270°$ without changing the polar behavior. The azimuth peak slightly shifts over frequency, due to the varying electrical length of the balun feedline.

B. ISM-Band Antenna

The principle of the antenna operation for the 2.45 GHz variant is the same, but the feeding network is different. Fig. 5 shows the feed-side of the antenna at a scale of 1:1, the dipole layer can be seen through the FR-4 PCB with dimensions $70 \times 70 \times 0.8$ mm. Here, the first section of transmission line from the central SMA connector to the PIN diodes is a 50-Ω line so no impedance transformation occurs. Two parallel PIN diodes each short three of the four arms for normal operation. From this point, a high-impedance $\lambda/4$ line connects to one arm of the dipole. Its high-impedance matches the dipole feed point to the 50-Ω line. The balanced lines connected to the dipole elements are shorted at $\lambda/4$, thus in combination with the second high-impedance part of the feed line, which bridges the gap near the dipole, they act as a balun. The DC bias for the diodes is again applied using a quarter wavelength line. The bypass capacitor at the dipole feed point and the diodes are soldered on extended pads so that the exact position of these elements can be fine tuned for production tolerances of the PCB material to achieve optimum matching.

III. Frequency Selective Surface Design

The design goal for this FSS is to create a high-impedance plane when placed between the antenna and the metal body floor pan of the car, thus removing the shorting effect of the ground plane. This FSS should also conserve key parameters such as efficiency and a low-elevation angle of the antenna beam. A promising approach is to design an AMC, which has a phase response of 0° for incident plane waves. Periodic structures allow the propagation of surface waves or spoof plasmons [15]–[17], which can degrade the antenna. We decided to base this design on mushroom-shaped unit cells that are proven to feature a stop band and to suppress surface waves [9], [10]. Depending on the permittivity of the substrate and the ground plane separation distance, the classical Sievenpiper mushroom unit cells extend up to almost a quarter wavelength. Interesting antenna designs as in [14] use these rather large FSS patches, but here the antenna element acts more like a feed to the periodic patch resonator array. We used techniques similar to [18], [19] by implementing meanders in the unit cell design to reduce its size [20], [21]. To obtain two independent controllable resonances, lumped capacitors are employed in one FSS design, as suggested in [22]. These lumped components further enhance flexibility of the AMC design.

We designed two variants of the AMC structures, called FSS1 and FSS2. Both are manufactured from two single-sided PCBs made of FR-4 with dimensions of $300 \times 300 \times 1.5$ mm. The copper layers from both PCBs face outside and nylon spacers with a height of 8 mm are used to separate the

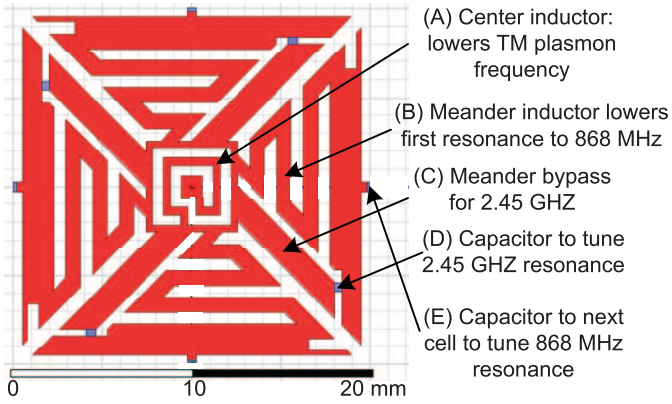

Fig. 6. Unit cell geometry of the designed AMC FSS1. Dark areas indicate top copper, capacitor positions shown in gray.

PCBs. So the overall dimensions of a single AMC panel are $300 \times 300 \times 11$ mm. We found that less separation between the PCBs reduces the bandwidth of the AMC, so 8-mm separation distance was chosen as a compromise between bandwidth and physical height. The lower PCB acts as a ground plane, and the copper layer of the top PCB is structured to form the unit cells of the AMC.

The top layer of the unit cell of FSS1 is shown in Fig. 6. In the center of the unit cell, a tinned copper wire with 0.51 mm diameter connects to the ground plane. The small planar inductor spiraling around the via does not lower the AMC resonance frequency, i.e., the frequency where the 0° phase reflection occurs. Rather, the center ground path for the AMC is essential to suppress transverse magnetic (TM) surface waves. The inductor, therefore, lowers the TM spoof plasmon frequency [15] or widens the band gap for TM waves. Transverse electric (TE) waves are not altered by the central inductor or the via.

To reduce the size of the unit cell, we partition the outer area of the cell in four sectors which are all identically constructed. We use meander inductors [(B) in Fig. 6] in every sector to lower the first resonance frequency to the European RFID UHF-band at 866 MHz. The coupling to the next cell by fringing fields is reduced by shrinking the outer dimension of the unit cell, so the dominant capacitance between cells is the discrete capacitor on every cell edge (E) which connects to the next cell. This component also tunes the first resonance of the AMC structure. We used ceramic capacitors in 0402 package with $C_1 = 0.4$ pF. For the resonance at the ISM-band, we bypass the meander by means of the diagonal line (C) which runs from the center ring to a coupling capacitor C_2 (D) which couples to the cell edge bar. The width of this line and the capacitance $C_2 = 0.2$ pF sets the second resonance at 2.45 GHz. Capacitors C_1 and C_2 make the design of FSS1 relatively insensitive to the often variable permittivity of the FR-4 substrate, since they dominate the relevant capacitances when compared to those of fringing fields between cells or stubs.

For FSS2, we substituted the discrete capacitors for structures in the copper layer of the top PCB. The coupling capacitor to the next cell C_1 is simply substituted by reducing the gap between adjacent top cells to 1.1 mm. The second capacitor which tunes the 2.45 GHz resonance is replaced by a small single stub interdigital capacitor. FSS2 is, therefore, more

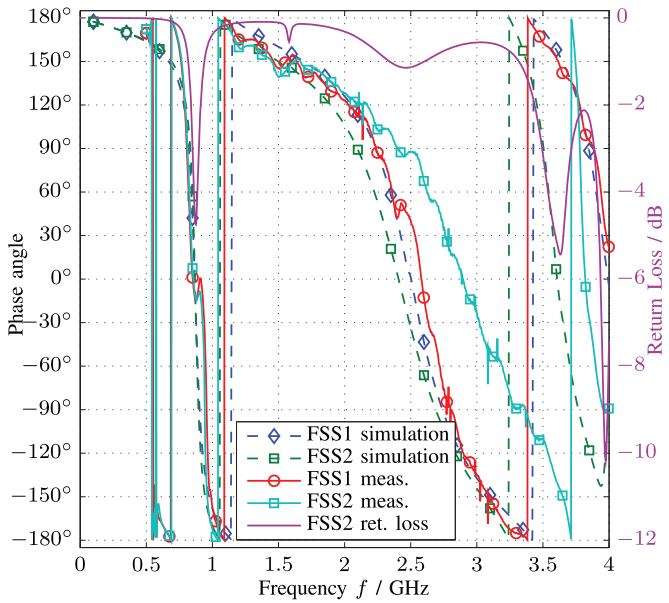

Fig. 7. Reflected phase of the designed AMC surfaces, showing simulation and measurement, and the simulated return loss of FSS2.

sensitive to substrate variations than FSS1. For a single AMC panel holding 15×15 unit cells approximately 1300 precision, capacitors are eliminated in this way.

A comparison of the phase response behavior of both FSS1 and FSS2 is shown in Fig. 7. The dashed lines show the simulation results of a single unit cell using master slave boundaries in HFSS. The relative bandwidth of the second resonance is 20%, while that of the first resonance is 9.8% in the case of FSS1, while the difference is even larger for FSS2 at 25% compared to 7.5%. This is beneficial, since the second resonance is more affected by the permittivity value of the substrate. Measurements also plotted in Fig. 7 were obtained in an anechoic chamber using the same methodology as in [9]. The AMC structure was placed on an absorber slab mounted on a wooden stand. Two identical ridged horn antennas were placed side by side facing the AMC structure at 61 cm distance. A slab of foam absorber was placed between the horns to reduce direct coupling, especially at higher frequencies. The horn antennas were connected to a vector network analyzer and the transmission coefficient was measured. For calibration, an equal-sized metallic reflector was placed at the exact same position. The phase response is obtained by subtracting the phases of the two measurements, and adding the known phase response of 180° for the metallic reflector. We see that the results from FSS1 are in close agreement with the simulation data. The phase response of FSS2 is slightly shifted toward higher frequencies for the second resonance.

Fig. 7 also shows the simulated return loss of FSS2 for plane wave excitation, including metal and substrate losses. At the lower design frequency of 865 MHz, the return loss is 4.4 dB, whereas the loss at 2.45 GHz is 1.1 dB. This plane wave characteristic does not directly relate to the application in the reactive near field of an antenna, but gives strong evidence that the designed AMC surfaces hold the intended properties of a somewhat lossy, phase-tuned reflector.

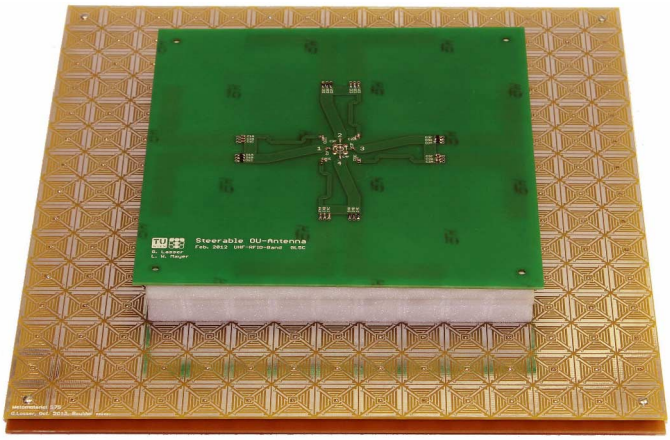

Fig. 8. UHF-SBA mounted atop FSS2 using foam spacers for a spacing of 28 mm (Setup 2b).

IV. Anechoic Chamber Measurements

In this section, we describe the pattern and efficiency measurements of an antenna system consisting of one variant of the SBA being mounted with foam spacers above FSS1 or FSS2, as shown in Fig. 8. The fundamental-analyzed antenna system geometries are shown in Fig. 9. We compare the radiation patterns of the SBA in free space to the ones obtained above either a reflector manufactured from copper or one of the AMC structures. To mimic the effects of the body floor pan, we use a circular ground plane with a diameter of 600 mm which is mounted directly below the FSS for particular measurements. Finally, for the UHF-band we also performed measurements on a FSS constructed by placing four panels of identical FSS2 structures beside each other, mounting them on the large circular ground plane. Two configurations were measured, such as the square arrangement and the "T" arrangement. Since both are asymmetric with respect to the mounting of the SBA, the selected beam which is indicated by roman numerals is important.

A. Return Loss Measurement Results

As the AMC surface for the complete antenna setup is placed in the reactive near field of the SBA, an influence on the return loss of the antenna is expected. The return loss of the UHF antenna is measured for four values of spacing between the SBA and FSS2 or a metal reflector of identical size, corresponding to the setups 1 to 4 specified in Table I. In Fig. 10, the free space return loss of the UHF-SBA is compared to two of these distances, Setup 1a with 12 mm separation and Setup 3a with 46 mm separation. The return loss degrades for both distances, if the SBA is mounted atop a metal reflector.

For the FSS and 46 mm of separation (Setup 3b) corresponding to 0.13 λ_0, the return loss in the operating band is increased. For frequencies up to 925 MHz, the return loss is increased as well, most likely because here surface waves are exited on the AMC structure. The return loss for Setup 2b (28 mm) is not shown here for clarity of the plot, but is similar to the one just described. For very close mounting of the FSS2 structure corresponding to 12 mm separation or 0.03 λ_0, the return loss again starts to degrade and two new resonances below the normal operation frequency appear. This is caused by detuning of some of the unit cells of the AMC structure due to the close dipoles of the SBA, causing different resonances for the different unit cells. The return loss behavior for FSS1 was found to be very similar to the one of FSS2 for all measured separation distances.

B. UHF-Band Pattern Measurement Results

The following measurements of the UHF-SBA plus AMC structure assembly were taken in an anechoic chamber using a spherical near field scanning system. Since our intended application is the mounting of this assembly on the body floor pan of a car, we seek for an overall assembly with low height, while keeping the elevation angle of the main beam as low as possible and without too much degradation of the efficiency. The relative efficiency of the overall antenna system is defined as

$$\eta_{\mathrm{r}} = \frac{\eta}{\eta_0} \tag{1}$$

where η is the efficiency of the antenna assembly (with FSS) and η_0 is the efficiency of the SBA in free space. Both efficiencies include the matching losses, so we refer to efficiency as the ratio of total radiated power and available power at the antenna input. In Fig. 11, η_{r} is plotted for different separations and configurations. As expected, the efficiency decreases for antenna positions close to the metallic reflector. For the observed frequency range, the efficiency degradation is almost constant and much larger than the matching loss introduced by detuning. For FSS2, the efficiency is frequency dependent, which is clear due to the narrow-band behavior of FSS2 as discussed in Section III. For Setup 4b at 880 MHz, there is even a small positive gain in efficiency, most likely caused by better matching. For the other scenarios, there are losses induced by FSS2, but for many frequencies the overall efficiency is better than the one using the metal reflector of the same size. When we compare the measurements of Setups 2b and 2c [adding the large circular ground plane (GP) underneath the FSS], we see only a minor degradation in efficiency which is 0.5 dB at maximum. Therefore, the size of a single AMC panel with 0.87 $\times$ 0.87 λ_0 is sufficient to effectively shield the SBA from the GP with respect to overall antenna efficiency. For FSS1 the situation is very similar, except that the efficiency curves are shifted approximately 20 MHz toward higher frequencies.

For Setup 2, which seems to be a reasonable compromise between assembly height and efficiency, we plot the normalized gain patterns in Fig. 12 for three mounting scenarios of the SBA: Setup 2a mounted above the metal reflector sized as the FSS2, Setup 2b mounted atop FSS2, and Setup 2c mounted atop the FSS2 plus the large circular GP. The gain plots are individually normalized and logarithmically show the gain corresponding to the electric field in φ direction, where φ is the azimuth angle measured in the x/y-plane and θ is the polar angle measured from the z-axis. As these plots show beam I, the desired main lobe is at $\varphi = 90°$. The azimuth plots Fig 12(a)–(c) are shown for $\theta = 27°$, since this corresponds to the polar peak of Setup 2c at the design frequency [see Fig. 12(e)]. In the

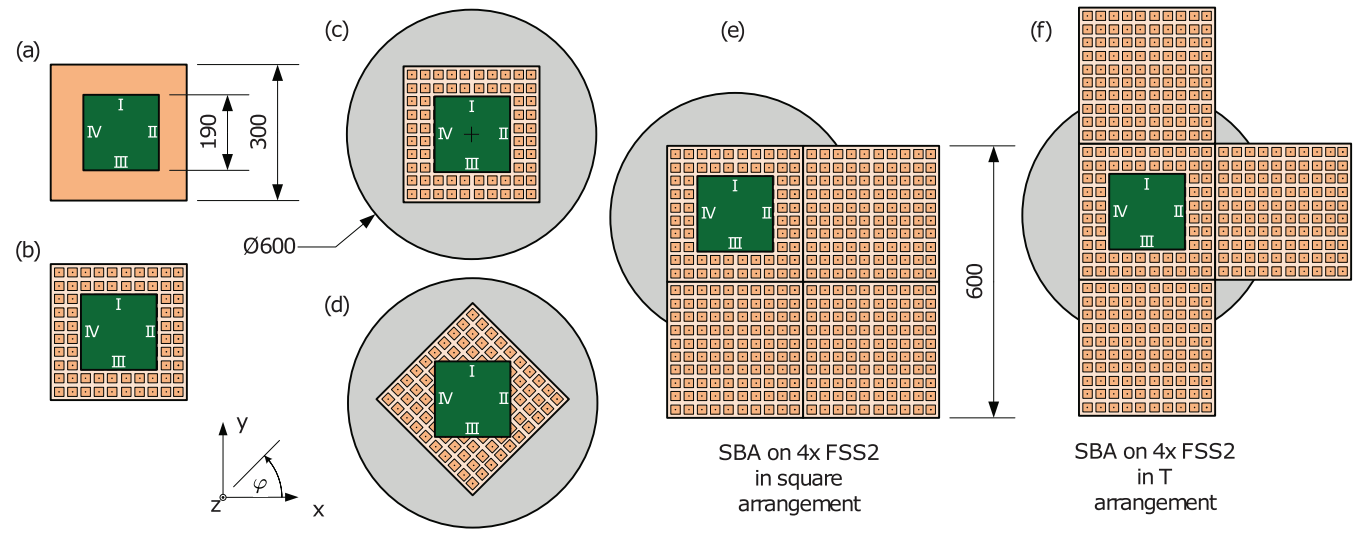

Fig. 9. Schematic representation of the different measurement Setups, dimensions given in mm. The green (dark) square indicates the position of the SBA, the roman numerals in it indicate the beam numbers of the SBA. (a) SBA atop the reflector, (b) SBA atop a FSS, (c) SBA atop a FSS plus a ground plane, (d) as (c) but with twisted FSS, (e) SBA mounted atop 4 FSS2 panels in square arrangement, (f) on SBA mounted above 4 FSS2 panels in "T" arrangement.

TABLE I
USED MEASUREMENT SETUPS

	Setup 1	Setup 2	Setup 3	Setup 4	Setup 5	Setup 6	Setup 7	Setup 8	Setup 9	Setup 10
Distance (mm)	12	28	46	74	18	20	24	34	40	60
Distance ($\lambda_{0,\mathrm{UHF}}$)	0.03	0.08	0.13	0.21	0.05	0.06	0.07	0.10	0.12	0.17
Distance ($\lambda_{0,\mathrm{ISM}}$)	0.10	0.23	0.38	0.60	0.15	–	–	–	–	–

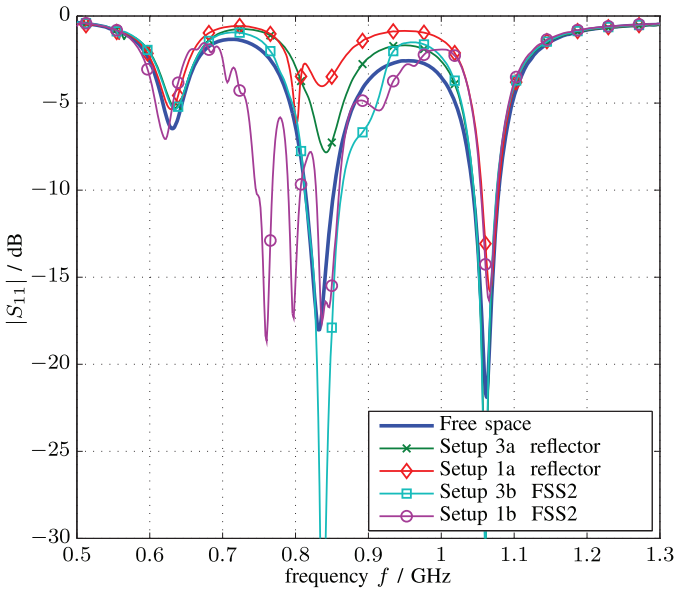

Fig. 10. Return loss of UHF-SBA mounted atop either a metal reflector or FSS2 at different heights according to Table I. The thicker line without markers shows a free space measurement of the SBA for comparison. The design frequency band is 865–868 MHz.

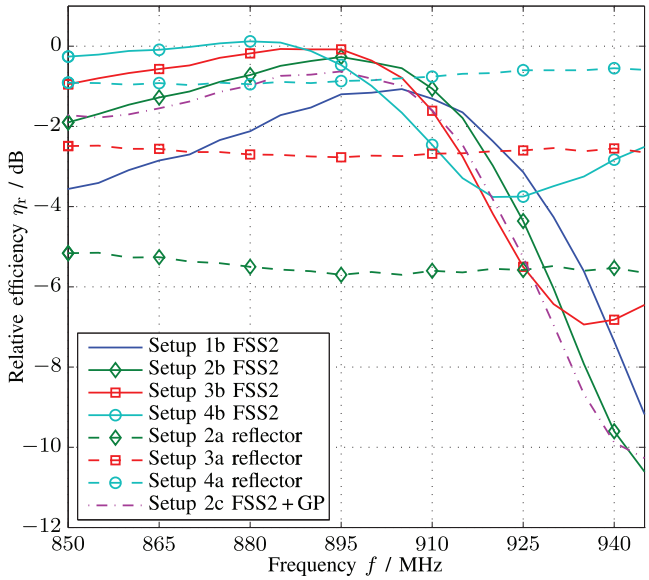

Fig. 11. Relative efficiency of the SBA mounted atop different substrates in four different heights when compared to the SBA in free space, according to Table I and Fig. 9.

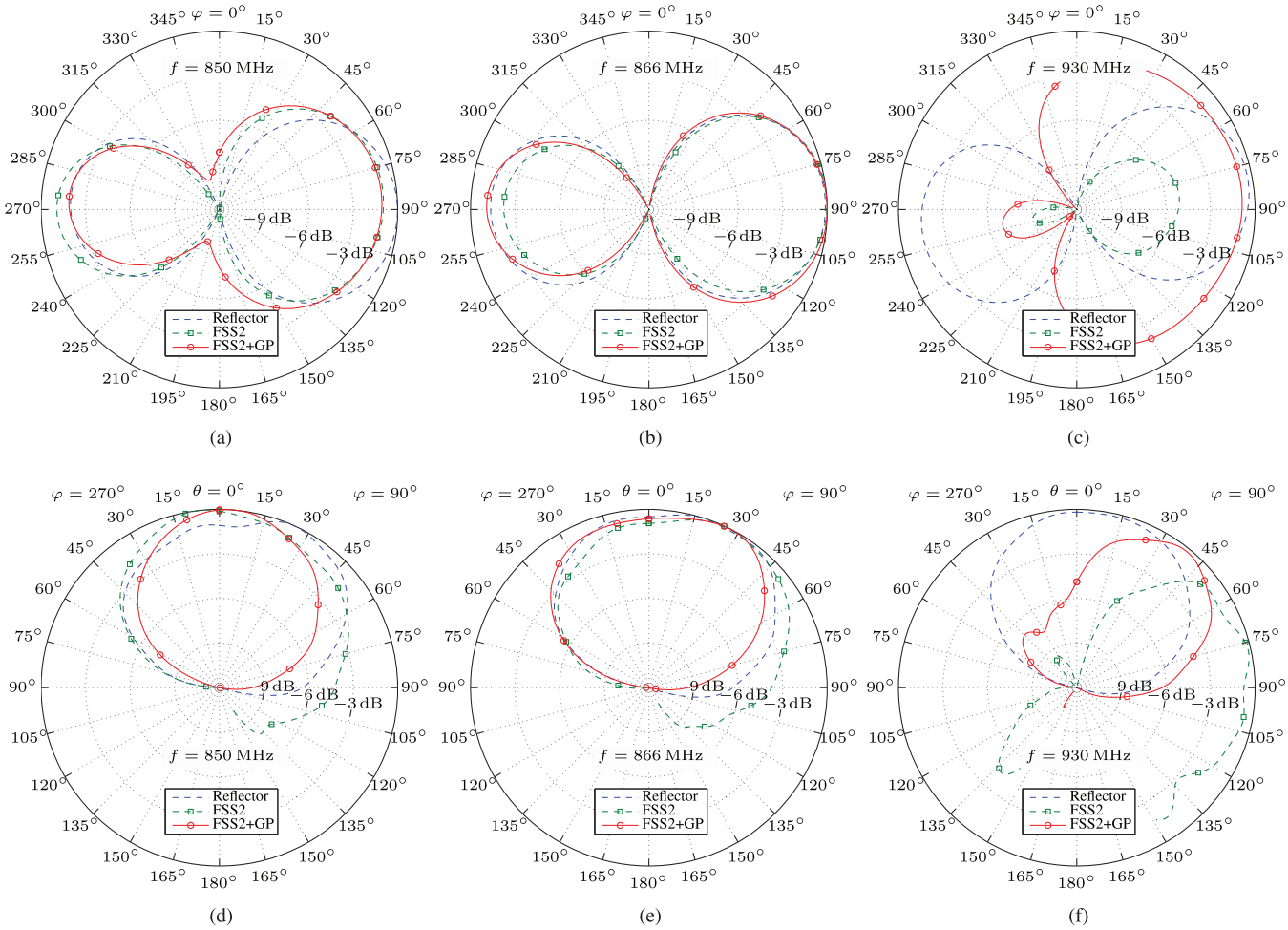

Fig. 12. Comparison of normalized gain patterns for beam I corresponding to E_φ for the UHF-SBA separated 28 mm to: Reflector (Setup 2a), FSS2 (Setup 2b), and FSS2 plus large circular GP (Setup 2c). Azimuth cuts at $\theta = 27°$ for (a) 850 MHz; (b) 866 MHz (b); and (c) 930 MHz. (d)–(f) Polar cuts at $\varphi = 90°$ and $\varphi = 270°$ for the same frequencies.

polar plots, Fig. 12(d)–(f), we see that adding a GP to the SBA raises the elevation angle and reduces the front-to-back ratio of the antenna. When the three mounting scenarios are compared, the scenario using just the FSS2 as substructure creates the lowest elevation angle with considerable radiation between $\theta = 60°$ and $\theta = 90°$, but this effect is not usable in practice as adding the circular GP will alter the gain pattern toward lower polar angles. We see that a single AMC panel at UHF is large enough to shield the antenna with respect to efficiency, but not regarding the radiation pattern. If the frequency is increased to 930 MHz as in Fig. 12(c) and (f), the SBA plus FSS2 assembly starts to behave as if the FSS2 structure would not be there. The radiation is also directed to the lower hemisphere and the peak of the main beam is close to $\theta = 90°$. Of course, this effect vanishes if the circular GP is added, still the front-to-back ratio exceeds the values of the pure SBA. In this frequency band, the FSS supports leaking TE surface waves and we assume that they influence the front-to-back ratio and elevation angle.

Results for FSS1 are similar to the results discussed for FSS2 with respect to the gain pattern. However, since the efficiency is shifted toward higher frequencies it is possible to create a pattern behavior similar to the FSS2 pattern in Fig. 12(f) with an efficiency penalty of just 1 dB compared to the pure SBA. Furthermore, at 910 MHz the pattern of the SBA using FSS1 as a substructure is also similar to the one using FSS2, but here even an efficiency improvement of 0.5 dB relative to the pure SBA is found.

The elevation angle of the different assemblies is further studied in Fig. 13. The plot shows the polar peak position θ_P conditioned that the peak is in the forward direction—thus it is at $\varphi = 90°$. Interestingly, larger FSS2-SBA separation distances lead to lower elevation angles. This behavior would be expected for a regular GP or perfect electric conductor (PEC), but not for an AMC. We see that this holds for the entire observed frequency range, but higher frequency values lead to polar peak positions θ_P with lower elevation angles. When the frequency is further increased, the reverse beam becomes stronger than the forward beam, and the corresponding line is truncated. For the preferred Setup 2, we see that twisting the FSS by 45° corresponding to Fig. 9(d) leads to high polar peak values despite the presence of the ground plane.

We conducted further measurements to see if a larger substructure improves the radiation pattern at UHF. A pattern comparison for various assemblies, especially including the

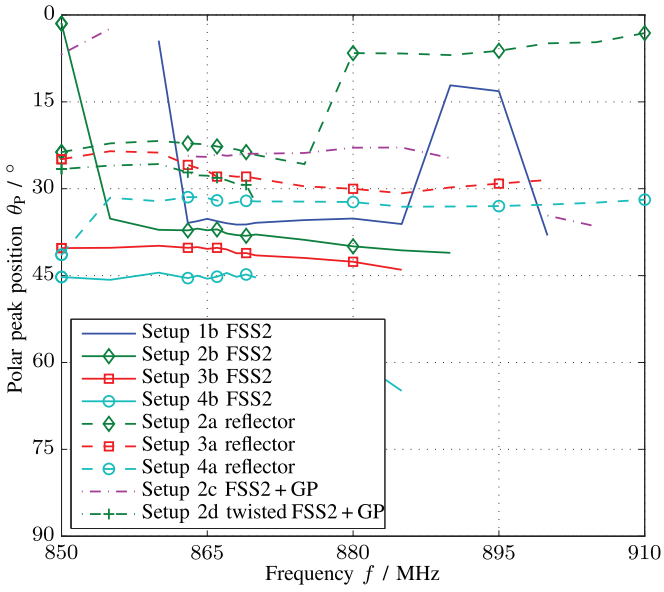

Fig. 13. Polar peak position of the SBA mounted atop different substrates in four different heights when compared to the SBA in free space. The different setups correspond to SBA-FSS-spacings according to Table I and configurations drawn in Fig. 9. The lines are truncated for frequencies where the reverse beam peaks are larger than the forward beam ones.

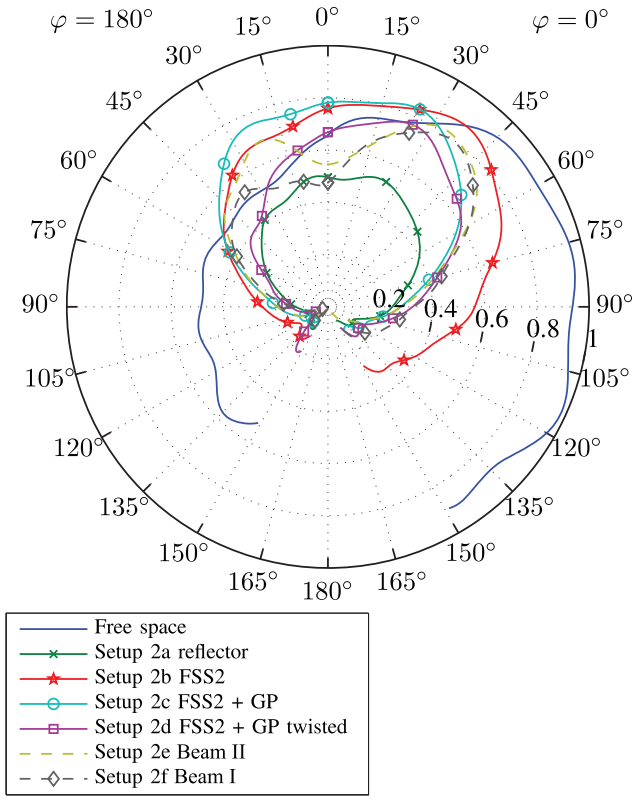

Fig. 14. Thetacut for SBA at 865 MHz atop different substrates in 28 mm separation and configurations according to Fig. 9 for Beam II except where noted otherwise. The radiation plots are normalized to the peak value of the SBA in free space. The region $\theta > 150°$ is not plotted here due to mechanical limitation of our measurement hardware.

variants (d)–(f) of Fig. 9, is shown in Fig. 14 at the design frequency of the SBA. Angles larger $\theta > 150°$ are not drawn since here our spherical measurement system does not produce satisfactory results due to its limited θ arm swing range. The pattern plots are jointly normlized for the global peak, so relative efficiencies are included, and the effects of losses in antenna, FSS, and due to mismatch are observed. The SBA backed on the reflector performs worst, it radiates almost omnidirectional to the upper hemisphere with a low-relative efficiency $\eta_r = -5.3$ dB. The degradation of the pattern due to the circular GP is observed when comparing Setups 2b and 2c. Setup 2d shows a better front-to-back ratio and slightly more radiation for $60° < \theta < 90°$. The efficiency penalty here is 1.6 dB to the pure SBA. Lower main peak angles are achieved with a larger AMC structure as the two last curves show. Interestingly, for the main peak an additional FSS2 panel in opposite of the selected beam direction does not improve the elevation angle (Setup 2e), but it enhances the front-to-back ratio. In the "T" configuration (Setup 2f), beam I has its polar peak at $\theta_P = 38°$ with an efficiency penalty of 1.8 dB.

C. ISM-Band Pattern Measurement Results

A sinlge AMC panel of 300 × 300 mm electrically is a large structure at 2.45 GHz ($2.45\,\lambda_0 \times 2.45\,\lambda_0$), and therefore, little effect of the large circular GP is expected. This was verified by measurements. In fact, the results for the setups corresponding to Fig. 9(b) and (c) are almost identical, so we only present Setup 2c corresponding to our relevant use case. Gain plots for three frequencies are shown in Fig. 15, for a spacing of 28 mm or 0.23 λ_0. Surprisingly, these results for almost a quarter wavelength separation are beneficial to the ones in Setup 1 ($0.1\ \lambda_0$), both in efficiency and in elevation angle. This shows that the simple prediction of the behavior of the ISM-SBA plus the FSS according to the AMC model and the measured 0° phase response for a plane wave incident (Fig. 7) does not accurately describe the radiation mechanisms of the antenna plus FSS assembly. An eigenwave analysis (shown in [21] for FSS1) provides more insight and confirms the stopband behavior, but since the FSS is in the near field of the antenna, only a full wave simulation of the SBA and the FSS would accurately predict the system behavior. At the time of FSS design (fall 2013), this was infeasible due to memory constraints on the available computers. Although the phase response of the FSS alone is not a perfect way to describe the AMC's behavior, the slightly different phase responses of FSS1 and FSS2 (Fig. 7) allow to understand the cause of the pattern differences seen in Fig. 15.

In Setup 1, both FSSs outperform the reflector in terms of efficiency by more than 1 dB. In Setup 2, at the design frequency, both assemblies show beams with directivity values of 10.1 and 10.2 dB, for FSS1 and FSS2, respectively. The peak of the main beam is at $\theta_P = 50°$. For both AMC surfaces, the efficiency penalty to free space operation is just 0.5 dB. The reflector performs identical in terms of efficiency, but a higher (undesired) elevation angle is observed. At 2.8 GHz, FSS2 is operated at the measured AMC resonance frequency and the radiation pattern becomes slightly more confined in θ. FSS1 at

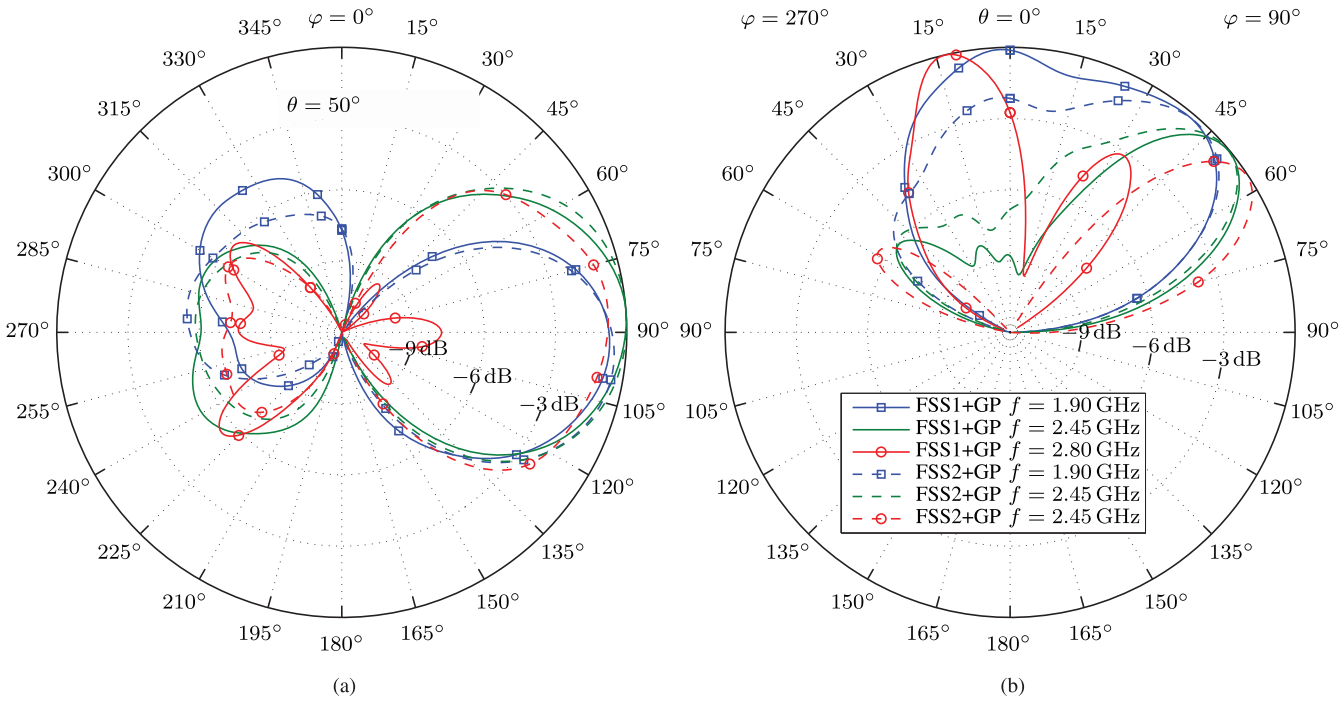

Fig. 15. Normalized gain patterns for beam I corresponding to E_φ in Setup 2c (28 mm separation) for the ISM-SBA assembly atop FSS1+GP (solid lines) or FSS2+GP (dashed lines) for three different frequencies f. Azimuth cut (a) drawn for $\theta = 50°$; polar cut (b) for $\varphi = 90°$ and $\varphi = 270°$.

the same frequency is already operated outside the AMC bandwidth (see Fig.7 and the pattern shows a reverse beam pointing toward low θ values.

V. Conclusion

In this contribution, we present the design and measurement of dual-band FSS structures that reduce the negative effects of a large ground plane on an SBA. The design is targeted for applications where an antenna needs to be placed under the body floor pan of a vehicle. The presented compact SBA antenna variants for the 868 MHz UHF-band and 2.45 GHz allow a beam to be steered in one of the four azimuth quadrants. Two dual-band AMC structures, FSS1 and FSS2, are presented, with unit cell dimensions of 0.058 λ_0 at UHF and 0.163 λ_0 at the ISM-band and relative AMC bandwidths of 7.5% at UHF and 25% in the ISM-band for FSS2. The use of discrete components in FSS1 yields to bandwidths of 9.8% and 20% while keeping the design insensitive to permittivity variations of the substrate. Based on this design method, we were able to present phase response measurements for the FSS1 type AMC which follow the designed values extremely well although the unpredictable but cost economic substrate FR-4 had been used.

Measurements of the various SBA plus substructure assemblies reveal that the relatively small AMC structure with an edge length of 0.87 λ_0, spaced 0.08 λ_0, effectively shields the SBA from a metal ground plane providing an efficiency enhancement to the mounting above metal of 3.7 dB at UHF. The optimum radiation pattern at the design frequency of 868 MHz using a single AMC structure panel was found for a 45° slanted orientation of the AMC resulting in a peak value at $\theta_P = 27°$ and a −3 dB forward polar angle of $\theta_{-3\ \mathrm{dB}} = 65°$. A lower main beam at $\theta_P = 38°$ is achieved using a larger AMC structure by concatenating four AMC panels. Above the design frequency similar peak values were observed for a single AMC panel, here the FSS itself and its edges act as a radiator. At the ISM-band, a high directivity of 10.2 dB, good front-to-back ratios and a high polar angle at $\theta_P = 50°$ were achieved with an efficiency improvement of 3.7 dB. In this band, the effects of the ground plane below the FSS are negligible.

References

[1] M. D. Brzeska, "RF modelling and characterization of tyre pressure sensors and vehicle access systems," Ph.D. dissertation, Karlsruher Institut für Technologie, Karlsruhe, Deutschland, 2013.

[2] F. Braghin, M. Brusarosco, F. Cheli, A. Cigada, S. Manzoni, and F. Mancosu, "Measurement of contact forces and patch features by means of accelerometers fixed inside the tire to improve future car active control," *Veh. Syst. Dyn.*, vol. 44, no. Suppl. 1, pp. 3–13, 2006.

[3] M. J. Matilainen and A. J. Tuononen, "Intelligent tire to measure contact length in dry asphalt and wet concrete conditions," *Proc. Int. Symp. Adv. Veh. Control (AVEC)*, Seoul, South Korea, 2012, vol. 12, pp. 1–6.

[4] J. Grosinger, L. W. Mayer, C. F. Mecklenbräuker, and A. L. Scholtz, "Determining the dielectric properties of a car tire for an advanced tire monitoring system," *Proc. IEEE 70th Veh. Technol. Conf. (VTC 2009-Fall)*, Sep. 2009, pp. 1–5.

[5] G. Lasser and C. F. Mecklenbräuker, "Channel model for tyre pressure monitoring systems (TPMS)," in *Proc. 4th Eur. Conf. Antennas Propag. (EuCAP'2010)*, Barcelona, Spain, Apr. 2010, pp. 1–5.

[6] G. Lasser and D. Löschenbrand, and G. Lasser and C. F. Mecklenbräuker, "Near field scans of tyre mounted dipoles using a separate phase reference antenna," in *Proc. IEEE-APS Top. Conf. Antennas Propag. Wireless Commun.*, Palm Beach, Aruba, Aug. 2014, pp. 612–615.

[7] G. Lasser, R. Langwieser, F. Xaver, and C. F. Mecklenbräuker, "Dual-band channel gain statistics for dual-antenna tyre pressure monitoring RFID tags," in *Proc. IEEE Int. Conf. RFID*, Orlando, FL, USA, Apr. 2011, pp. 57–61.

[8] G. Lasser, L. W. Mayer, and C. F. Mecklenbräuker, "Compact low profile UHF switched-beam antenna for advanced tyre monitoring systems," in *Proc. IEEE-APS Top. Conf. Antennas Propag. Wireless Commun.*, Sep. 2012, pp. 732–735.
[9] D. Sievenpiper, L. Zhang, R. F. Jimenez Broas, N. G. Alexopolous, and E. Yablonovitch, "High-impedance electromagnetic surfaces with a forbidden frequency band," *IEEE Trans. Microw. Theory Techn.*, vol. 47, no. 11, pp. 2059–2074, Nov. 1999.
[10] A. P. Feresidis, G. Goussetis, S. Wang, and J. Y. C. Vardaxoglou, "Artificial magnetic conductor surfaces and their application to low-profile high-gain planar antennas," *IEEE Trans. Antennas Propag.*, vol. 53, no. 1, pp. 209–215, Jan. 2005.
[11] J. Sahaya Kulandai Raj, J. Bonney, P. Herrero, and J. Schoebel, "A reconfigurable antenna for MIMO application," in *Proc. Loughborough Antennas Propag. Conf. (LAPC)*, Nov. 2009, pp. 269–272.
[12] V. A. Nguyen and P. S. Ook, "Compact switched and reconfigurable 4-ports beam antenna array for MIMO applications," in *Proc. IEEE MTT-S Int. Microw. Workshop Ser. Intell. Radio Future Pers. Terminals (IMWS-IRFPT)*, Aug. 2011, pp. 1–3.
[13] J. Sahaya Kulandai Raj, J. Fahlbusch, and J. Schoebel, "A beam switching three layer reconfigurable antenna," in *Proc. 7th German Microw. Conf. (GeMiC)*, Mar. 2012, pp. 1–4.
[14] P. Deo, A. Mehta, D. Mirshekar-Syahkal, P. J. Massey, and H. Nakano, "Thickness reduction and performance enhancement of steerable square loop antenna using hybrid high impedance surface," *IEEE Trans. Antennas Propag.*, vol. 58, no. 5, pp. 1477–1485, May 2010.
[15] J. Pendry, L. Martin-Moreno, and F. J. Garcia-Vidal, "Mimicking surface plasmons with structured surfaces," *Science*, vol. 305, no. 5685, pp. 847–848, Aug. 2004.
[16] M. J. Lockyear, A. P. Hibbins, and J. R. Sambles, "Microwave surface-plasmon-like modes on thin metamaterials," *Phys. Rev. Lett.*, vol. 102, no. 7, p. 073901, Feb. 2009.
[17] A. Byers, I. Rumsey, Z. Popović, and M. Piket-May, "Surface-wave guiding using periodic structures," in *Proc. IEEE Antennas Propag. Soc. Int. Symp.*, 2000, vol. 1, pp. 342–345.
[18] M. F. Abedin, M. Z. Azad, and M. Ali, "Wideband smaller unit-cell planar ebg structures and their application," *IEEE Trans. Antennas Propag.*, vol. 56, no. 3, pp. 903–908, Mar. 2008.
[19] D. J. Kern, D. H. Werner, A. Monorchio, L. Lanuzza, and M. J. Wilhelm, "The design synthesis of multiband artificial magnetic conductors using high impedance frequency selective surfaces," *IEEE Trans. Antennas Propag.*, vol. 53, no. 1, pp. 8–17, Jan. 2005.
[20] G. Lasser, "Passive RFID for automotive sensor applications," Ph.D. dissertation, Technische Universität Wien ,Vienna, Austria, Oct. 2014.
[21] G. Lasser, Z. Popović, and C. F. Mecklenbräuker, "Dual-band, low-frequency artificial magnetic conductor using lumped components," in *Proc. 9th Int. Congr. Adv. Electromagn. Mater. Microw. Opt.—Metamater.*, Oxford, U.K., Sep. 2015, pp. 175–177.
[22] M. Bray and D. Werner, "A novel design approach for an independently tunable dual-band EBG AMC surface," in *Proc. IEEE Antennas Propag. Soc. Int. Symp.*, Jun. 2004, vol. 1, pp. 289–292.

Gregor Lasser (S'09–M'15) received the Dipl.-Ing. and the Dr. Techn. degrees in electrical engineering (both with distinction) from Vienna University of Technology, Vienna, Austria, in 2008 and 2014, respectively.

Since 2014, he has served as the Vice President of the Telecommunication Cercle, Vienna, Austria. Since 2015, he has been a Research Associate with the University of Colorado Boulder, Boulder, CO, USA, where he is working on broadband envelope tracking power amplifiers and compact intelligent antenna systems.

Dr. Lasser received the second position of the EEEfCOM Innovation Award in 2008 for the RFID testbed developed during his Diploma thesis and the Faculty Award of the Faculty of Electrical Engineering and Information Technology, Vienna University of Technology for the presentation of his Doctoral dissertation entitled "Passive RFID for Automotive Sensor Applications."

Lukas W. Mayer was born in Vienna, Austria. He received the Ph.D. degree in electrical engineering (*summa cum laude*) from Vienna University of Technology, in 2009.

During his Diploma studies at the Vienna University of Technology, Vienna, Austria, he developed components of the radio-frequency frontend of the institute's multiple-input multiple-output (MIMO) testbed. In his thesis, he analyzed the properties of radio channels typical for radio-frequency identification (RFID) systems and presents two advanced antenna designs that enable multistandard and multifrequency operation. Furthermore, he developed new antenna measurement methods that allow accurate characterization of small and autonomous antennas. From 2010 to 2011, he served as the Head of R&D with the startup company PIDSO GmbH, Vienna, Austria, where he built ultra-lightweight antennas and antenna systems made of carbon-fiber composites for unmanned air- and ground-vehicles. Since 2012, he has been with Siemens AG Österreich, Austria, where he developed radio-frequency solutions for the company's wide research and product range. In 2014, he was appointed as a Senior Key Expert for antennas, wireless sensors, and RFID.

Zoya Popović (S'86–M'90–SM'99–F'02) received the Dipl.Ing. degree in electrical engineering from the University of Belgrade, Serbia, Yugoslavia, in 1985, and the Ph.D. degree electrical engineering from the California Institute of Technology, Pasadena, CA, USA, in 1990.

Since 1990, she has been with the University of Colorado Boulder, Boulder, CO, USA, where she is currently a Distinguished Professor and holds the Hudson Moore Jr. Endowed Chair with the Department of Electrical, Computer, and Energy Engineering. She was named the 2015 Distinguished Research Lecturer of the University of Colorado Boulder. In 2001/2003 and 2014, she was a Visiting Professor at the Technical University of Munich, Munich, Germany, and ISAE, Toulouse, France, respectively. Since 1991, she has guided 50 Ph.D. students and currently leads a group of 15 doctoral students and four postdoctoral fellows. Her research interests include high-efficiency transmitters for radar and communication, low-noise and broadband microwave and millimeter-wave circuits, antenna arrays, wireless powering for batteryless sensors, and medical applications of microwaves such as microwave core-body thermometry and travelling-wave MRI.

Prof. Popović was elected a Foreign Member of the Serbian Academy of Sciences and Arts in 2006. In 2013, she was named IEEE MTT Distinguished Educator and an NSF White House Presidential Faculty Fellow in 1993. She was the recipient of the 1993 and 2006 IEEE MTT-S Microwave Prizes for the best journal papers, the 1996 URSI Issac Koga Gold Medal, and a 2000 Humboldt Research Award for Senior U.S. Scientists from the German Alexander von Humboldt Stiftung and the 2001 Hewlett-Packard(HP)/American Society for Engineering Education (ASEE) Terman Medal for combined teaching and research excellence.

Christoph F. Mecklenbräuker (S'88–M'97–SM'08) received the Dipl.-Ing. degree (with distinction) in electrical engineering from Vienna University of Technology, Vienna, Austria, in 1992, and the Dr.-Ing. degree in electrical engineering (with distinction) from Ruhr University Bochum, Bochum, Germany, in 1998.

From 1997 to 2000, he was with Siemens, Vienna, Austria. From 2000 to 2006, he has held a Senior Research Position with Telecommunications Research Center Vienna (FTW), Vienna, Austria. In 2006, he joined the Faculty of Electrical Engineering and Information Technology, Vienna University of Technology, Vienna, Austria, as a Full Professor. Since 2009, he has been leading the Christian Doppler Laboratory for Wireless Technologies for Sustainable Mobility, Vienna University of Technology. His research interests include vehicular connectivity, ultrawideband radio, and multiple-input multiple-output techniques for wireless systems.

Dr. Mecklenbräuker is a member of the European Association for Signal Processing. His doctoral dissertation on matched field processing received the Gert Massenberg Prize in 1998.